Supplementary Information

Eutectic-electrolyte-enabled zinc metal batteries towards wide temperature and voltage windows

Xue Bai,‡[ab] Mingzi Sun,‡[c] Jun Yang,[a] Bijian Deng,[d] Kai Yang,[a] Bolong Huang,*[c] Weiguo Hu,*[ab] and Xiong Pu*[ab]

[a] CAS Center for Excellence in Nanoscience, Beijing Key Laboratory of Micro-Nano Energy and Sensor, Beijing Institute of Nanoenergy and Nanosystems, Chinese Academy of Sciences, Beijing 101400, China

[b] School of Nanoscience and Engineering, University of Chinese Academy of Sciences, Beijing 100049, China

[c] Department of Applied Biology and Chemical Technology, The Hong Kong Polytechnic University, Hung Hom, Kowloon, Hong Kong SAR, China

[d] Institute for Applied Materials, Karlsruhe Institute of Technology, 76344 Eggenstein-leopoldshafen, Germany

‡ These authors contributed equally to this work.

* Correspondence: bhuang@polyu.edu.hk (B.H.),
huweiguo@binn.cas.cn (W.H.),
puxiong@binn.cas.cn (X.P.)

Experimental Section

Preparation of electrolytes and electrodes

Zinc bis(trifluoromethylsulfonyl)imide ($Zn(TFSI)_2$, 98%) and diethyl phosphoramidate (DEPA, 98%) were purchased from Bidepharm and Macklin, respectively. A series of electrolytes were prepared by stirring $Zn(TFSI)_2$ and DEPA with molar ratios of 1:6, 1:8, 1:10 and 1:12 at 25 °C for 2 h. The traditional 2 M $ZnSO_4$ aqueous electrolyte was selected as a control electrolyte. It was obtained by dissolving zinc sulfate ($ZnSO_4 \cdot 7H_2O$, Aladdin, AR) in deionized water. Zn foil with a thickness of 100 μm and a purity of 99.99% was used as Zn electrode. Cu foil with a thickness of 100 μm and a purity of 99.99% was used as Cu cathode. 5 mmol divanadium pentaoxide, 5 mmol potassium iodide, and 1.0 g urea were added to 50 ml deionized water, followed by concentrated sulfuric acid and stirred continuously. Then the stirred solution was transferred to a 100 ml autoclave and heated at 120 °C for 3 h. The sample was washed repeatedly and the V_2O_5 material was obtained by drying in an oven for 12 h. V_2O_5 material, Ketjen Black (KB), and polytetrafluoroethylene (PTFE) were mixed uniformly with ethanol in a weight ratio of 7:2:1. The obtained slurry was coated on a stainless-steel (SS) mesh and dried at room temperature for 3 h to prepare V_2O_5 pole piece. Then the pole piece was cut into a disk (Φ = 1 cm) shape as V_2O_5 cathode. Meanwhile, the same operation method was used to prepare activated carbon electrode for the capacitor with a mass ratio of 8:1:1. The mass loading of V_2O_5 electrode and activated carbon electrode is approximately 2 mg cm^{-2}.

Characterizations

The safety test is to place the separator wetted by DEE under an open flame lighter and observe its combustion. Differential scanning calorimetry (DSC) tests were performed using NETZSCH DSC 200F3, with an initial equilibrium temperature of −100 °C in a nitrogen atmosphere and a rate of 5 °C min^{-1} heating to 50 °C. Thermogravimetric analysis (TGA, METTLER TOLEDO TGA/DSC1) was conducted under nitrogen atmosphere in the temperature from 30 °C to 300 °C, with a heating rate of 10 °C min^{-1}. The conductivity and viscosity of DEEs were measured by a conductivity meter (ST3100M) and a rotational viscometer (NDJ-1). Fourier transform infrared (FTIR) spectra were collected by

VERTEX80v. Raman spectra of two components and DEEs were recorded on a Raman spectrometer (LabRAM HR Evolution) with a laser wavelength of 532 nm. The contact angle between solid and liquid interface was obtained using a contact angle tester (SDC-350) to evaluate the wetting free energy based on Equation 1.[1]

$$\Delta G = \frac{RT}{3} ln \frac{(1-\cos\theta_A)^2(2+\cos\theta_A)}{4} \quad (1)$$

where ΔG is the wetting free energy, R is the ideal gas constant, T is the thermodynamic temperature, and θ_A represents the contact angle.

The disassembled electrodes were rinsed with deionized water or anhydrous ethanol to remove any residual electrolyte and dried under vacuum at 40 °C for further analysis. X-ray diffraction (XRD) was performed on an equipment (Xpert3 Powder) with X-ray radiation wavelength of 1.5406 Å. The morphology of Zn nucleation and growth behavior in different electrolytes was collected using a scanning electron microscopy (SEM, SU8020). The composition of SEI layer was tested by in-depth X-ray photoelectron spectroscopy (XPS, Thermo Scientific K-Alpha). The depth of sputtered layer was calculated based on the sputtering rate and the duration of sputtering, with a depth of 5 nm corresponding to 18 s. Field emission scanning electron microscopy (FESEM, Helios NanoLab 600i) was used to perform focused ion beam (FIB) cutting and morphology observation on Zn electrode after cycling. The prepared thin section sample was further analyzed on SEI layer under a transmission electron microscopy (TEM, JEOL JEM-F200). The voltages used for SEM and TEM are 5 kV and 200 kV, respectively.

Electrochemical measurements

The linear scanning voltammetry (LSV) curves were measured using SS as working electrode, Zn foil as the counter electrode and reference electrode, at a scan rate of 1 mV s^{-1}. Tafel test was performed in a three-electrode system, with Ag/AgCl electrode as reference electrode. The nucleation and growth behavior of Zn in two electrolytes was observed in a cuvette battery. Zn−Zn symmetric cells, Zn−Cu cells, Zn−V_2O_5 full cells, and Zn-ion hybrid capacitors were assembled into LIR2032 coin cells. Zn−Zn symmetric cells in $ZnSO_4$ aqueous

electrolyte and DEE were tested at high and low current densities and areal capacities. In different electrolytes, the coulombic efficiency of Zn−Cu cells was measured with a cut-off potential of 1 V. The SEI-coated Zn foil was obtained after 50 cycles in DEE at a current density of 0.1 mA cm^{-2} with 0.1 mAh cm^{-2}. The cycling and rate performance of Zn−V_2O_5 full cells were measured with V_2O_5 as cathode, operating within the voltage range of 0.1 to 1.7 V. And the cycling and rate tests of all coin cells and capacitors were performed on LAND battery testing system (CT2001A). A single pouch cell was assembled by using Zn foil (4×5.5 cm^2) as anode, glass fiber as separator, V_2O_5 pole piece (4×5.5 cm^2) as cathode, and aluminum laminated film (ALF) for thermoplastic sealing. Zn−V_2O_5 pouch cells were interlinked in a cathode-anode configuration, and then packaged with ALF to obtain an internal series-connected pouch cell. The tests and application of cells at high and low temperatures were conducted in a constant temperature and humidity test chamber (GDJS-50L). The rate performance of Zn−Zn symmetric cells was tested with different current densities of 0.1, 0.5, 1, 2, 4, and 5 mA cm^{-2} at 80 °C, followed by cycling performance tests at 0.1 mA cm^{-2}. Similarly, at −20 °C, Zn−Zn symmetric cells were performed with different current densities of 0.01, 0.05, 0.1, 0.2, 0.4, and 0.5 mA cm^{-2}, and then the cycling performance was tested at 0.01 mA cm^{-2}. Cyclic voltammetry (CV) tests of Zn-ion hybrid capacitor were performed using a two-electrode system at a scan rate of 10 mV s^{-1} under different operating windows from 0.1 V to 2.5 V.

Zn electrocrystallization process

The electrocrystallization of Zn metal shares similarities with salt crystallization in supersaturated aqueous solutions and cooling crystallization of molten metal, both of which undergo two stages: nucleation and growth. Specifically, the electrocrystallization process of Zn occurs under an electric field driven by overpotential. This process involves a spontaneous transformation from an unbalanced state to an equilibrium state, leading to a decrease in the free energy of system, denoted by ΔG_1 (<0). And a new phase is generated to form a new interface, causing an increase in the free energy of system, represented by ΔG_2 (>0). Considering that the crystal structure of Zn is hexagonal close-packed (HCP), the total energy

change ΔG during Zn nucleation can be inferred from Equation 2.[2]

$$\Delta G = -\frac{3\sqrt{3}r^2h\rho nF\eta}{2M} + 6rh\sigma_1 + \frac{3\sqrt{3}r^2}{2}(\sigma_1 + \sigma_2 - \sigma_3) \quad (2)$$

where r is the nucleus radius, and h is the height of nucleus, ρ is the density of Zn, n is the number of electrons, and F is the Faraday constant, η is the overpotential, M is the relative atomic mass of Zn metal, σ_1, σ_2 and σ_3 represents the interfacial tension between nucleus and electrolyte, nucleus and electrode, and electrolyte and electrode, respectively. Taking Zn metal as electrode, $\sigma_1 = \sigma_3$ and $\sigma_2 = 0$. According to the principles of chemical thermodynamics, $\Delta G < 0$ is required for Zn nuclei to exist stably. It can be seen from Equation 2 that ΔG is a function of radius r. When $\frac{\partial \Delta G}{\partial r} = 0$, the critical nucleus radius r_c can be obtained.

Theoretical calculations

Density functional theory (DFT) calculations within the CASTEP package were introduced to investigate the interactions within DEE.[3] In particular, the generalized gradient approximation (GGA) with Perdew-Burke-Ernzerhof (PBE) functions was chosen to achieve accurate expressions of the exchange-correlation interactions.[4-6] Based on the ultrafine quality and selection of ultrasoft pseudopotential scheme, the corresponding plane-wave cutoff energy was set as 380 eV for geometry optimizations of all coordination configurations.[7] In the meantime, to guarantee optimizations, we chose coarse k-point settings and applied the Broyden-Fletcher-Goldfarb-Shannon (BFGS) algorithm for all energy minimization.[8, 9] The convergence criteria applied for geometry optimization were set as follows: the Hellmann-Feynman forces should not exceed 0.001 eV $Å^{-1}$ and the total energy and atomic displacement should be converged to smaller than 5×10^{-5} eV $atom^{-1}$ and 0.005 Å, respectively. The interaction energy $E_{interact}$ has been calculated based on the following Equation 3.

$$E_{interact} = E_{total} - xE_{Zn} - yE_{TFSI} - zE_{DEPA} \quad (3)$$

E_{total} represents the total energy of structure. x, y, and z denote the number of Zn^{2+}, $TFSI^{-}$, and DEPA in structure, respectively. E_{Zn}, E_{TFSI}, and E_{DEPA} indicate the energy of individual ions and molecules, respectively.

The molecular dynamic (MD) simulations were conducted in four different DEEs with $Zn(TFSI)_2$:DEPA molar ratios of 1:6, 1:8, 1:10, and 1:12. These electrolytes included 20 $Zn(TFSI)_2$ molecules with 120, 160, 200 and 240 DEPA molecules in the unit cells. The MD was carried out under the NVT condition in 298 K and 1 atm. The time step was 1fs and the total simulation time was set to 5 ps with 5000 simulation steps. The Noise scheme was selected for the thermostat. After MD simulations, we further carried out geometry optimizations to investigate the interaction energies. The diffusion coefficients (D) were calculated based on the following Equation 4.

$$D = \frac{1}{6}\frac{d}{dt}\left\langle \left| r_i(t) - r_i(0) \right|^2 \right\rangle \quad (4)$$

The value of $\frac{d}{dt}\left\langle \left| r_i(t) - r_i(0) \right|^2 \right\rangle$ corresponds to the slope of the linear fitting of MSD results vs time, which can be obtained by the linear fitting equation.

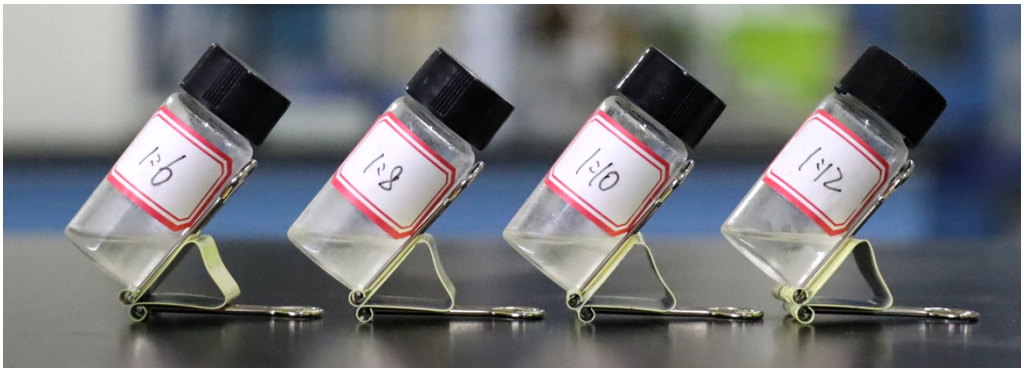

Fig. S1 The digital photo of DEEs with different $Zn(TFSI)_2$:DEPA molar ratios at −20 °C.

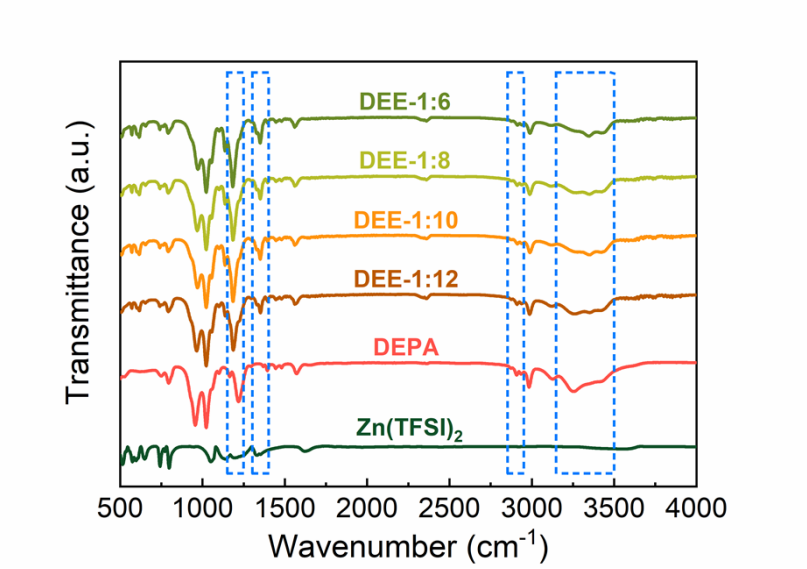

Fig. S2 FTIR spectra of two components and DEEs with different $Zn(TFSI)_2$:DEPA molar ratios (full spectra).

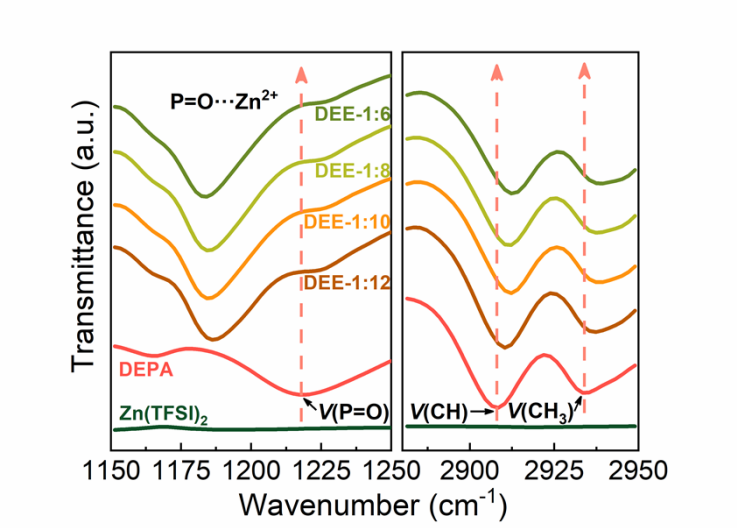

Fig. S3 FTIR spectra: ν(P=O), ν(CH) and ν(CH_3) of DEEs with different $Zn(TFSI)_2$:DEPA molar ratios.

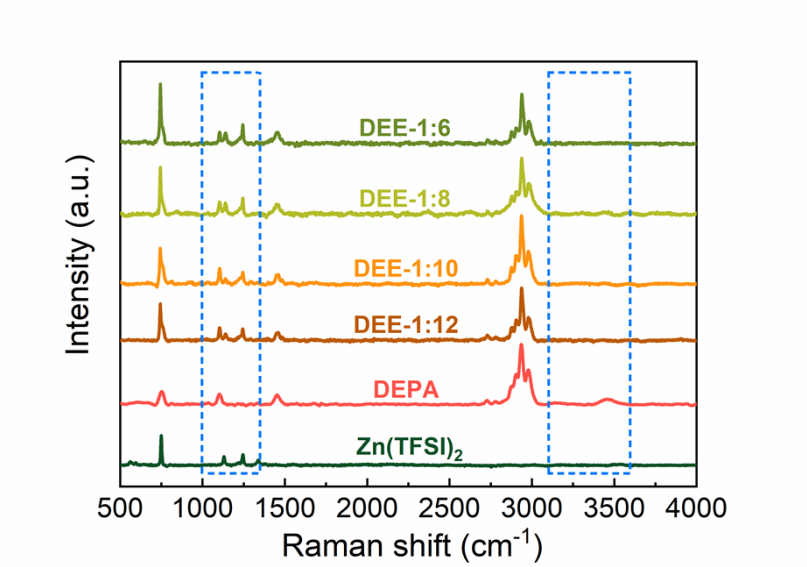

Fig. S4 Raman spectra of two components and DEEs with different $Zn(TFSI)_2$:DEPA molar ratios (full spectra).

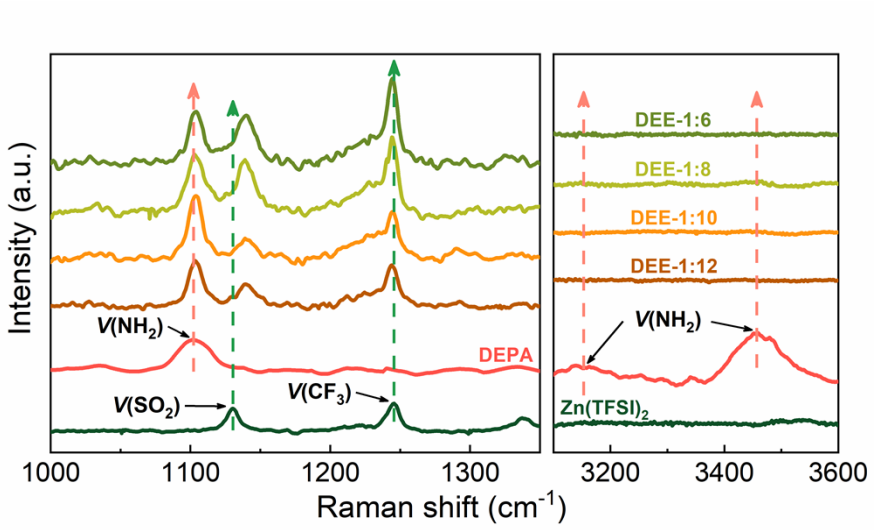

Fig. S5 Raman spectra: $\nu(NH_2)$, $\nu(SO_2)$ and $\nu(CF_3)$ of DEEs with different $Zn(TFSI)_2$:DEPA molar ratios.

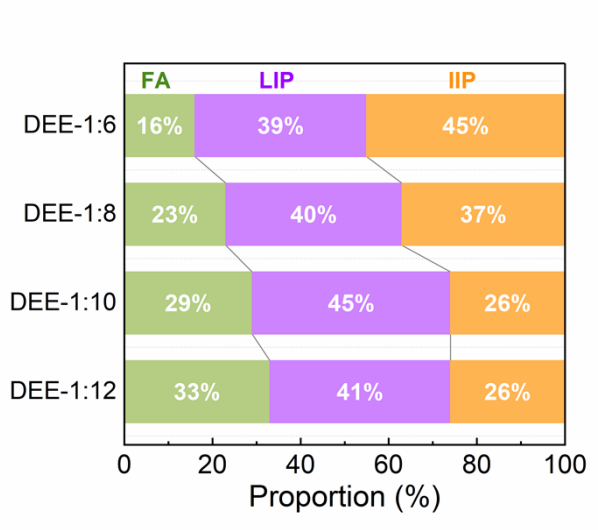

Fig. S6 The proportions of free anions (FAs), loose ion pairs (LIPs), and intimate ion pairs (IIPs) obtained from fitted Raman spectra of different DEEs.

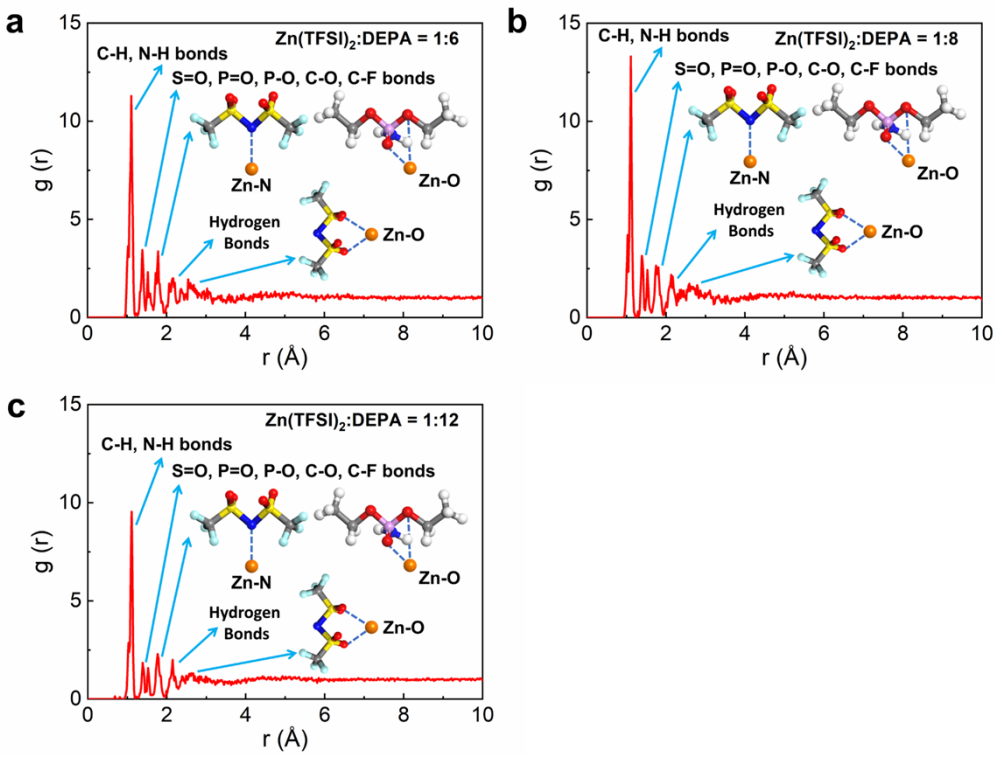

Fig. S7 The RDF of DEE with a $Zn(TFSI)_2$:DEPA molar ratio of (a) 1:6, (b) 1:8, and (c) 1:12.

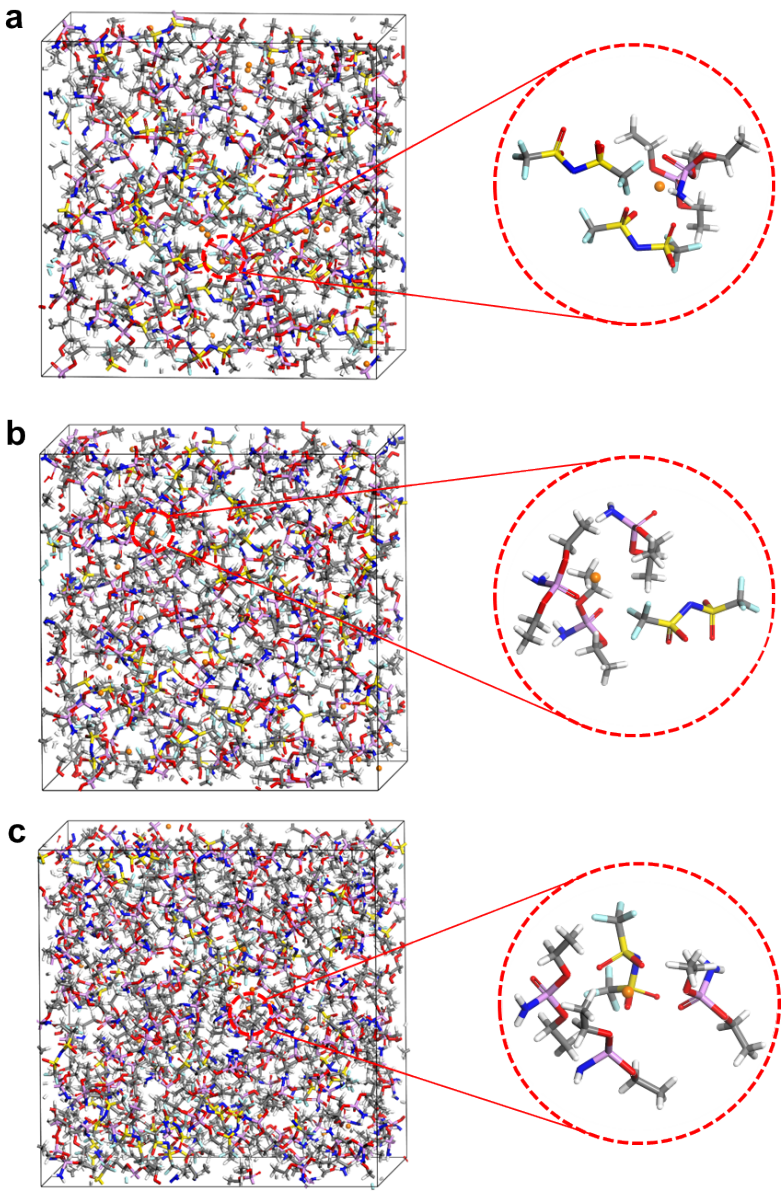

Fig. S8 The snapshot of DEE after MD simulations with a $Zn(TFSI)_2$:DEPA molar ratio of (a) 1:6, (b) 1:8, and (c) 1:12.

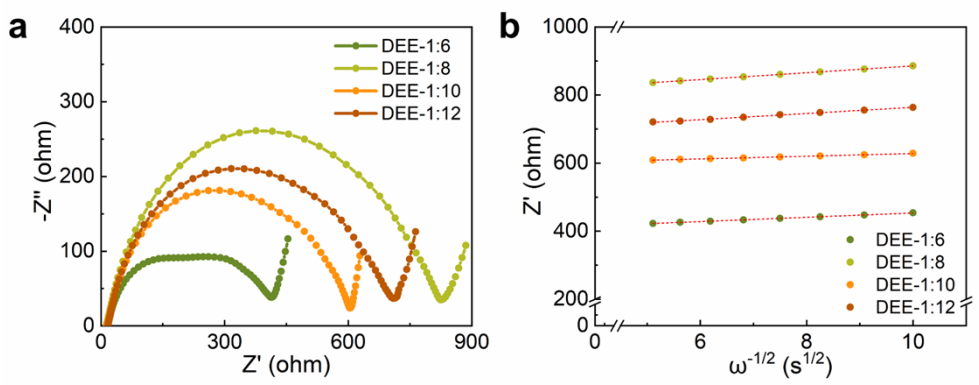

Fig. S9 (a) Electrochemical impedance spectroscopy (EIS) curves of Zn−V_2O_5 full cells with different DEEs. (b) Dependence of Z' vs. $\omega^{-1/2}$ based on EIS curves.

Note of Fig. S9: The diffusion coefficient of Zn^{2+} in DEE with different proportions can be obtained as

$$D = \frac{R^2T^2}{2A^2n^4F^4C^2\sigma^2} \tag{5}$$

where R is the gas constant, T is the temperature, A is the electrode area, n is the electron transfer number, F is the Faraday constant, and C is the concentration of Zn. σ is the Warburg coefficient, which can be obtained from the slope of the Z' and $\omega^{-1/2}$ plot in the impedance spectroscopy. These results obtained from EIS curves confirm that despite changes in electrolyte composition, the diffusion coefficient remains consistent within the same order of magnitude.

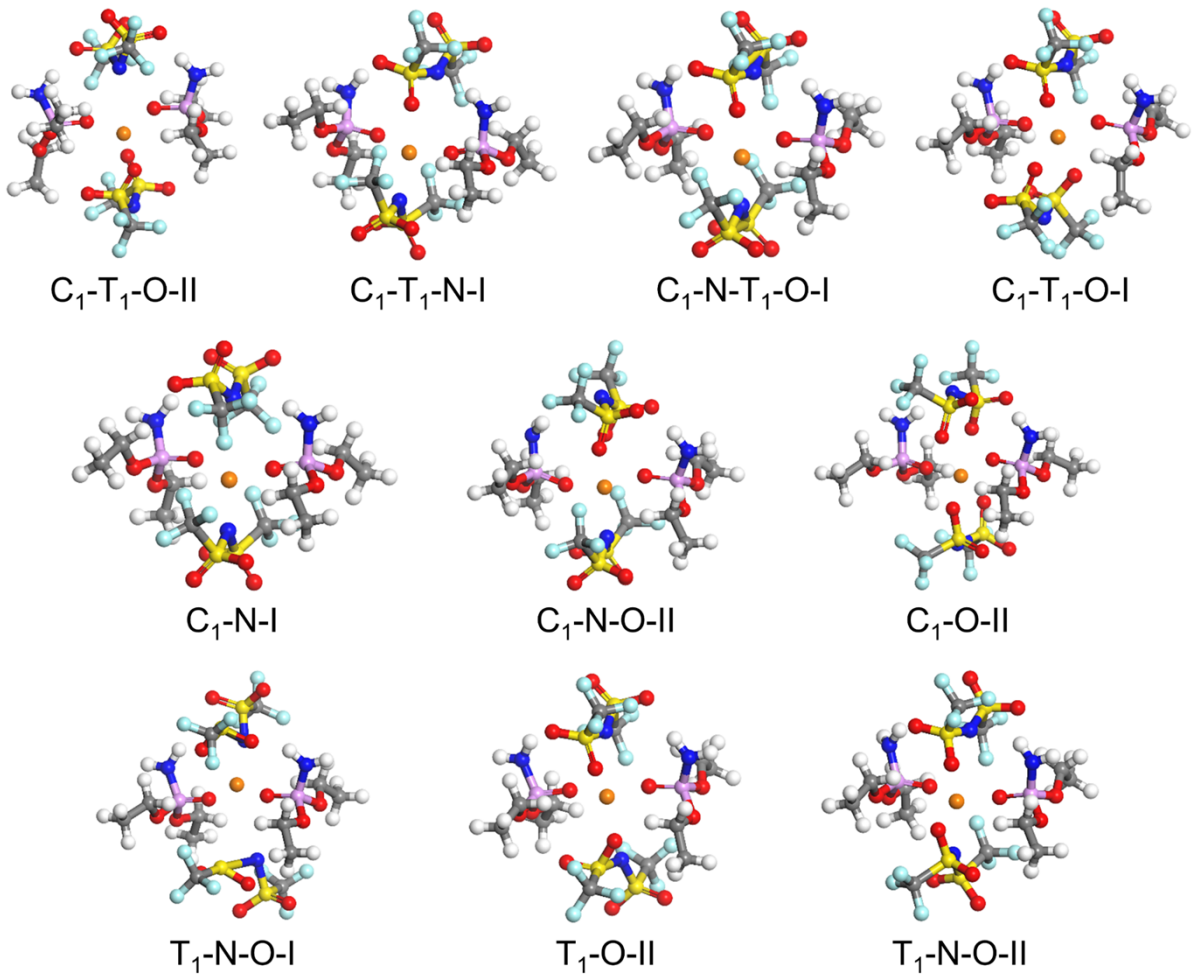

Fig. S10 The geometry configurations of [$ZnTFSI_2(DEPA)_2$] complexes. C_1 and T_1 indicate the cisoid and transoid form of $TFSI^-$, respectively. I: monodentate coordination of $TFSI^-$. II: bidentate coordination of $TFSI^-$. (Zn-orange, N-dark blue, S-yellow, O-red, C-gray, F-lake blue, P-purple, H-white.)

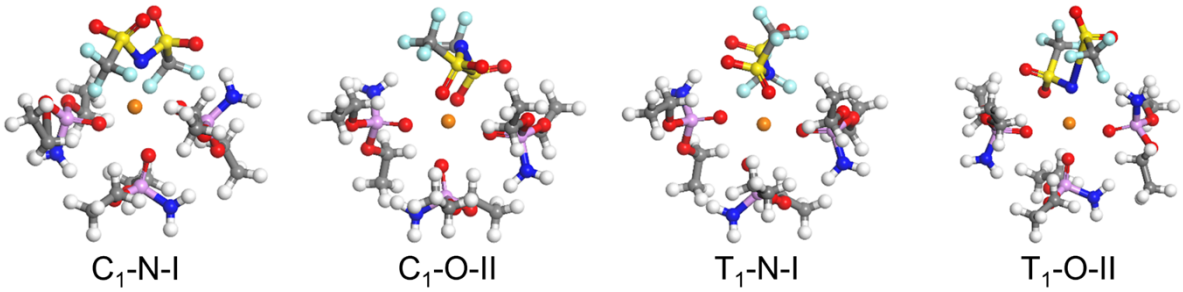

Fig. S11 The geometry configurations of $[Zn(TFSI)(DEPA)_3]^+$ complexes.

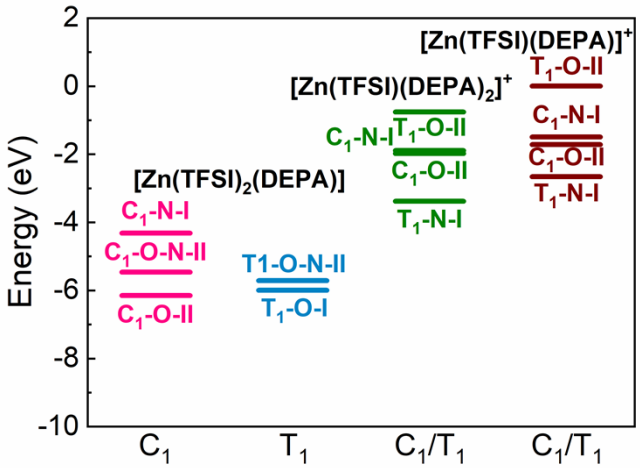

Fig. S12 The stability comparisons of coordination configurations for $[Zn(TFSI)_2(DEPA)]$, $[Zn(TFSI)(DEPA)_2]^+$ and $[Zn(TFSI)(DEPA)]^+$.

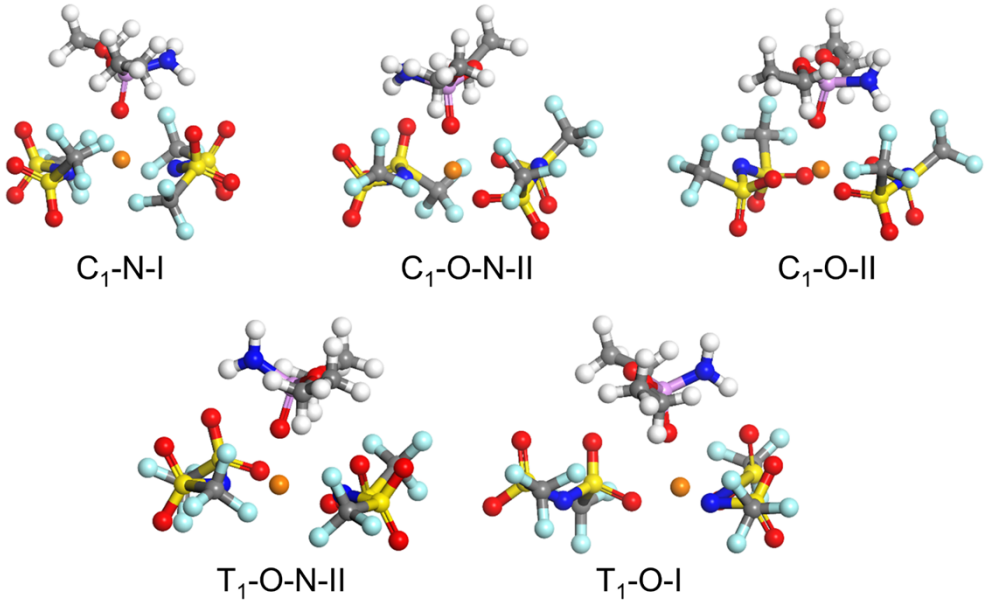

Fig. S13 The geometry configurations of [Zn(TFSI)$_2$(DEPA)] complexes.

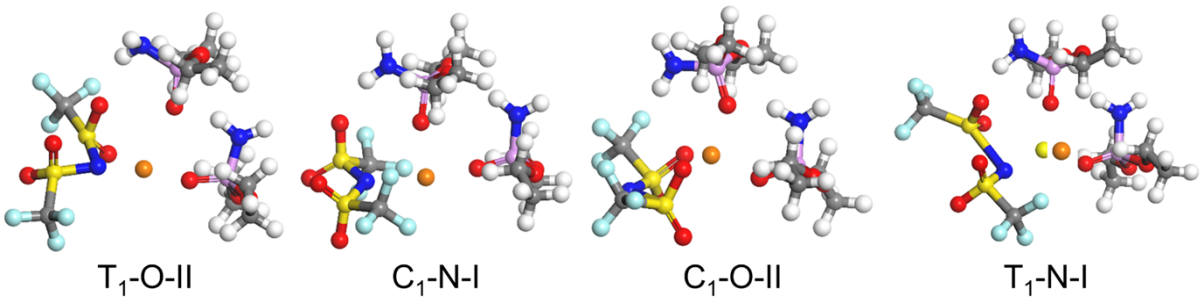

Fig. S14 The geometry configurations of $[Zn(TFSI)(DEPA)_2]^+$ complexes.

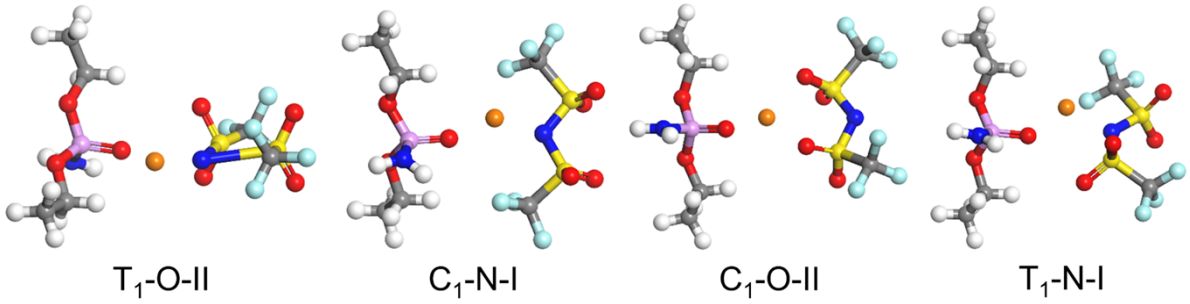

Fig. S15 The geometry configurations of $[Zn(TFSI)(DEPA)]^+$ complexes.

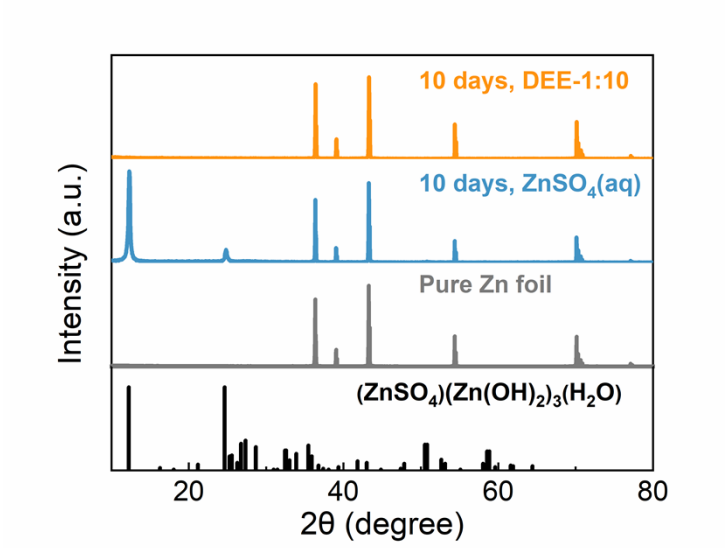

Fig. S16 Corresponding XRD patterns of Zn foil soaked in $ZnSO_4$ aqueous electrolyte and DEE-1:10 for 10 days, with the X-ray radiation wavelength of 1.5406 Å.

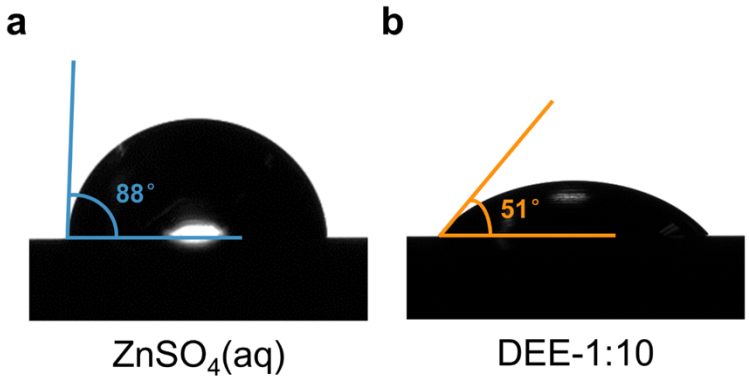

Fig. S17 The solid-liquid contact angle between Zn foil and (a) $ZnSO_4$ aqueous electrolyte and (b) DEE-1:10.

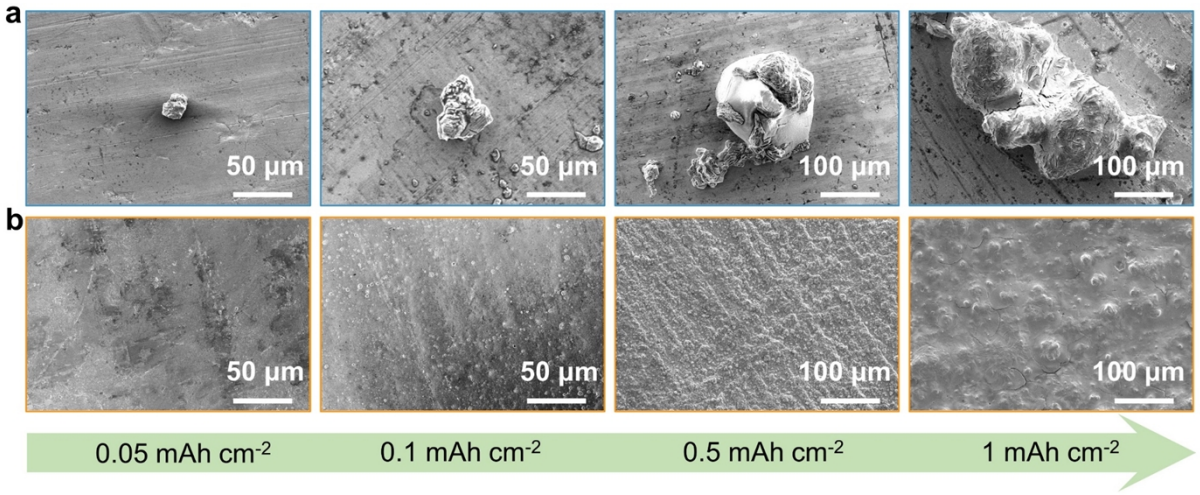

Fig. S18 SEM images of Zn nucleation and growth behavior at a current density of 0.1 mA cm^{-2} under different plating charge quantities (0.05~1 mAh cm^{-2}) in (a) $ZnSO_4$ aqueous electrolyte and (b) DEE-1:10.

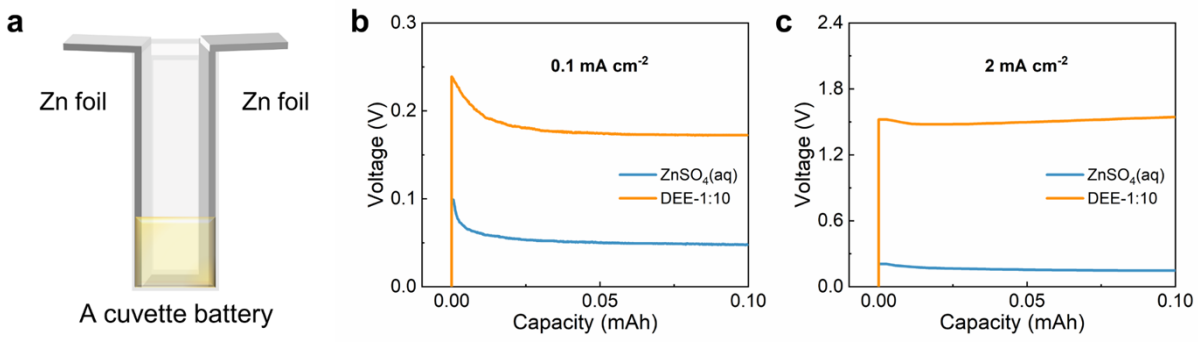

Fig. S19 (a) Schematic diagram of a cuvette battery for observing Zn nucleation and growth behavior. The voltage profiles of Zn electrode in two electrolytes at a current density of (b) 0.1 mA cm^{-2} and (c) 2 mA cm^{-2}.

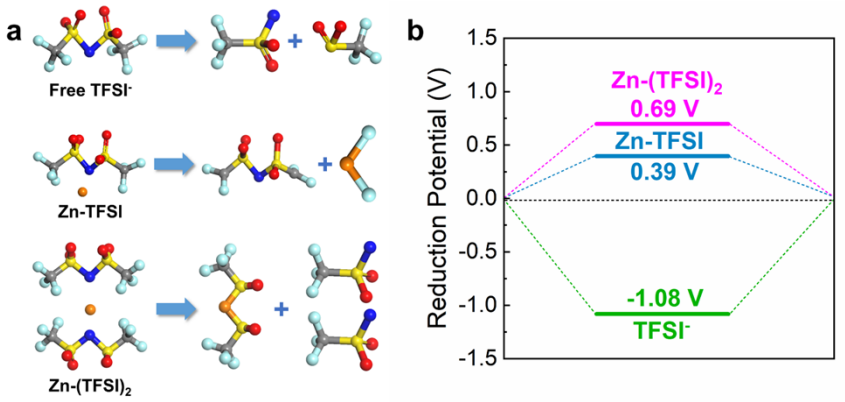

Fig. S20 (a) $TFSI^-$ reduction process in different coordination environments. (b) The reduction potential of $TFSI^-$ obtained through theoretical calculation.

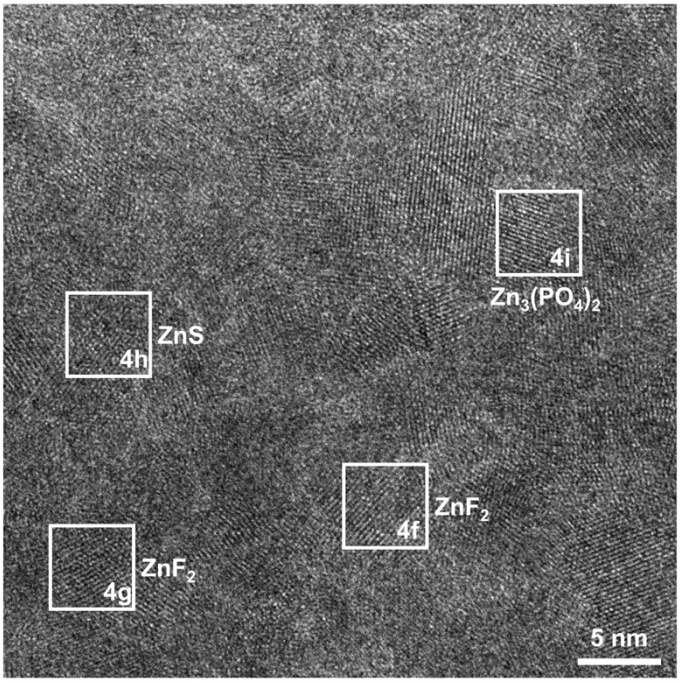

Fig. S21 HRTEM images of Zn anode after cycling in DEE-1:10.

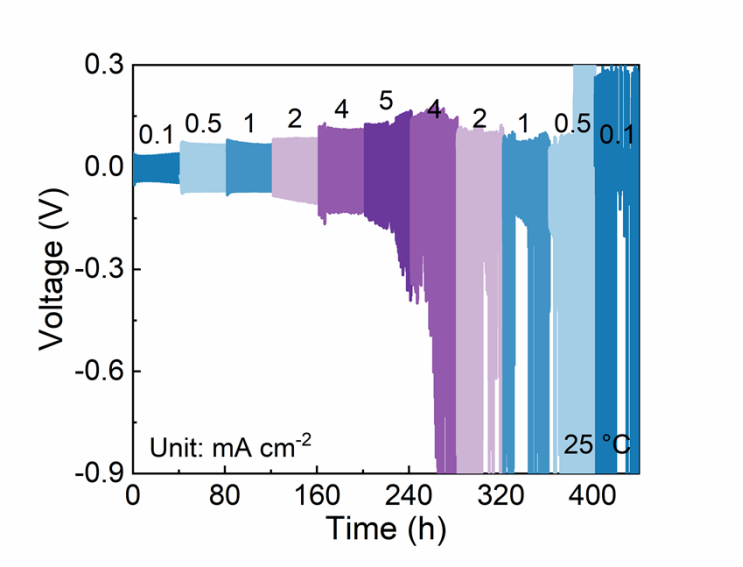

Fig. S22 Rate performance of symmetric cell in $ZnSO_4$ aqueous electrolyte at current densities of 0.1~5 mA cm^{-2}.

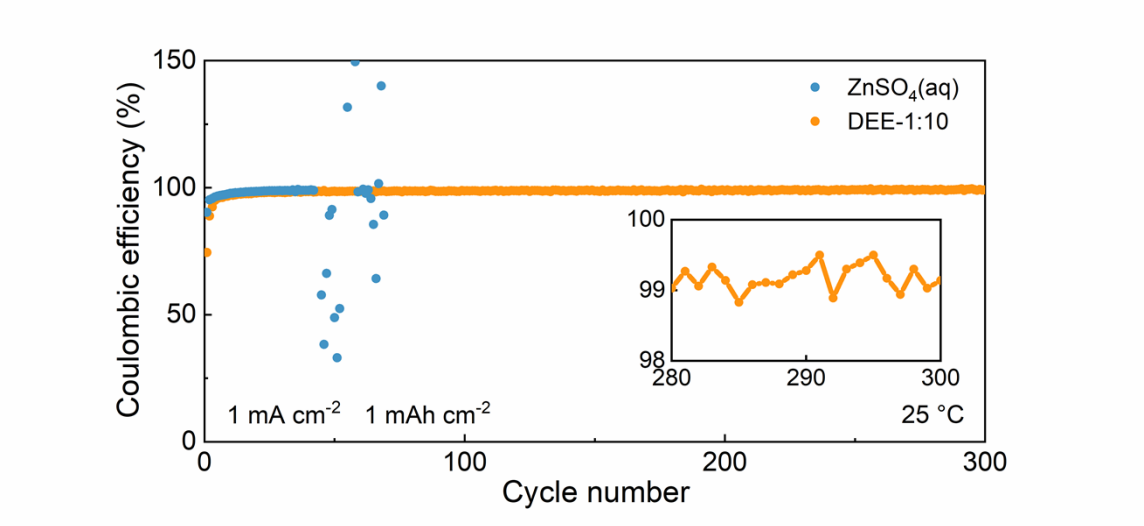

Fig. S23 Coulombic efficiency of Zn−Cu cells at a current density of 1 mA cm^{-2} with an areal capacity of 1 mAh cm^{-2} in two electrolytes.

Note of Fig. S23: Coulombic efficiency (CE) is a critical parameter for assessing the reversibility of Zn plating/stripping reaction. Zn−Cu cells in different electrolytes were tested at a current density of 1 mA cm^{-2} with an areal capacity of 1 mAh cm^{-2}. It can be observed that the Zn−Cu cell tested in $ZnSO_4$ aqueous electrolyte rapidly fails after 42 cycles with drastic fluctuations in CE, which may be caused by inhomogeneous Zn nucleation, as well as side reactions (HER and self-corrosion). However, Zn−Cu cell in DEE can achieve 300 stable cycles.

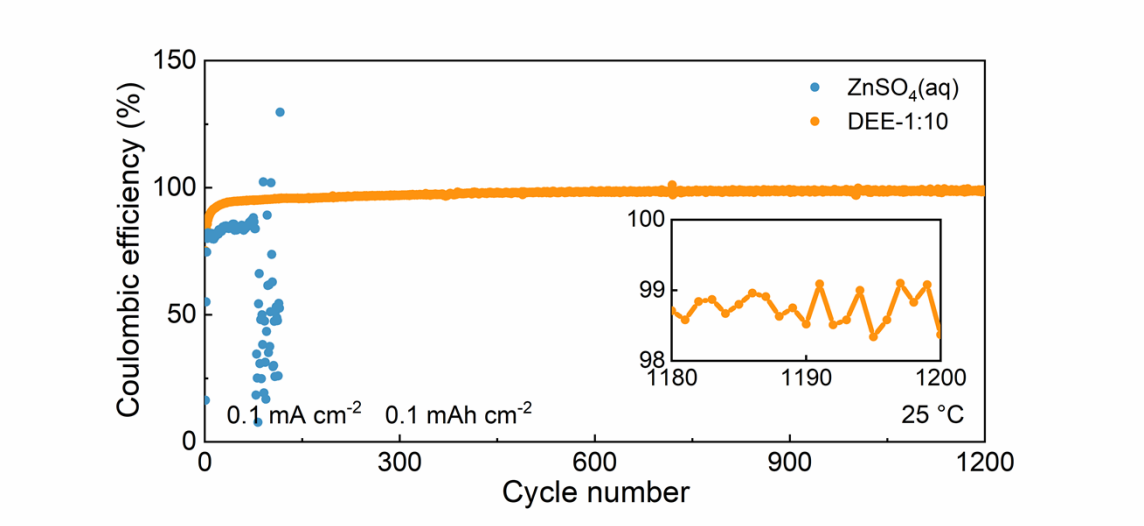

Fig. S24 Coulombic efficiency of Zn−Cu cells at a current density of 0.1 mA cm^{-2} with an areal capacity of 0.1 mAh cm^{-2} in two electrolytes.

Note of Fig. S24: At a low current density of 0.1 mA cm^{-2}, Zn−Cu cell in DEE achieves an average CE of 96% after completing 500 stable cycles. Conversely, the CE in $ZnSO_4$ electrolyte can only maintain 78 cycles and is as low as 82%. It is reconfirmed that even at a low current density, DEE can resist dendrite formation and side reactions, ultimately achieving superior reversibility of Zn plating/stripping process.

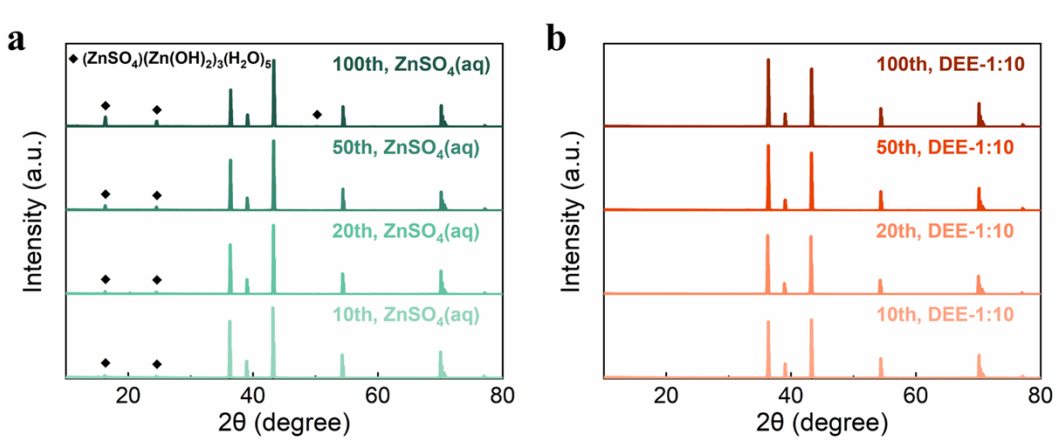

Fig. S25 Corresponding XRD patterns of Zn anode after cycling at 0.1 mA cm^{-2} with 0.1 mAh cm^{-2} in (a) $ZnSO_4$ aqueous electrolyte and (b) DEE-1:10, with the X-ray radiation wavelength of 1.5406 Å.

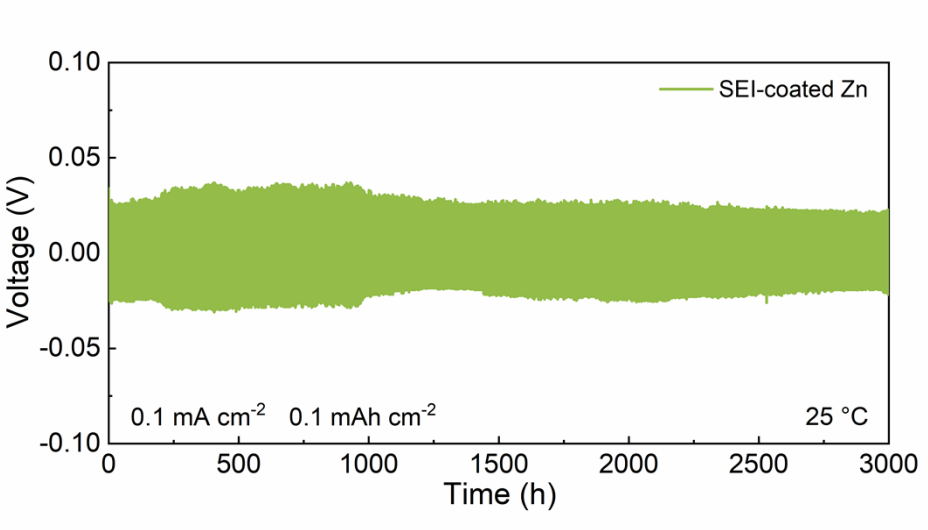

Fig. S26 Cycling performance of symmetric cells with SEI-coated Zn foil in $ZnSO_4$ aqueous electrolyte at a current density of 0.1 mA cm^{-2}.

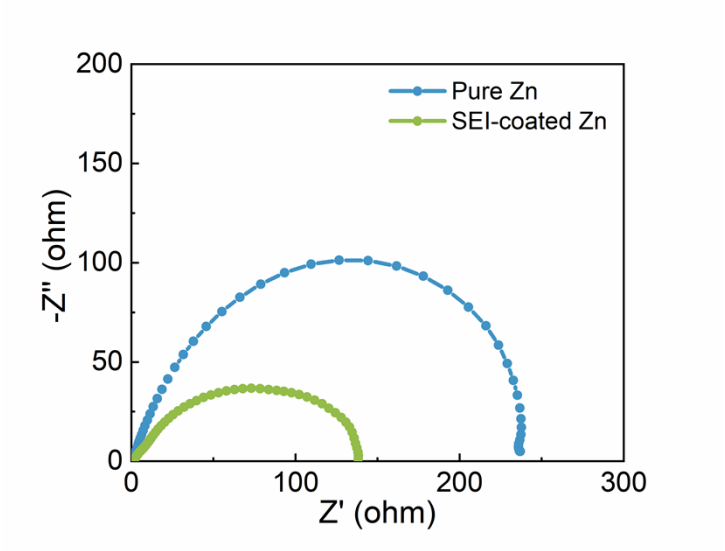

Fig. S27 Electrochemical impedance spectroscopy (EIS) curves of Zn–Zn symmetric cells with pure Zn and SEI-coated Zn foil in $ZnSO_4$ aqueous electrolyte.

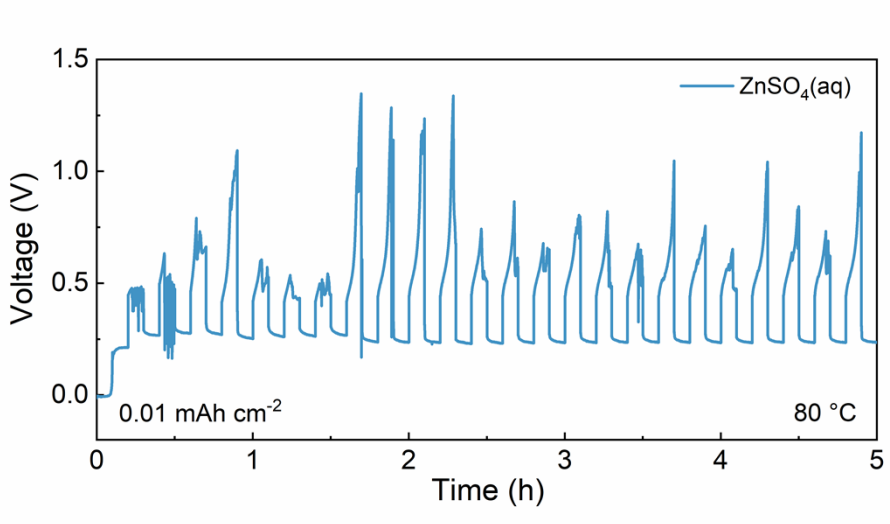

Fig. S28 The voltage profiles of Zn−Zn symmetric cell in $ZnSO_4$ aqueous electrolyte at 80 °C.

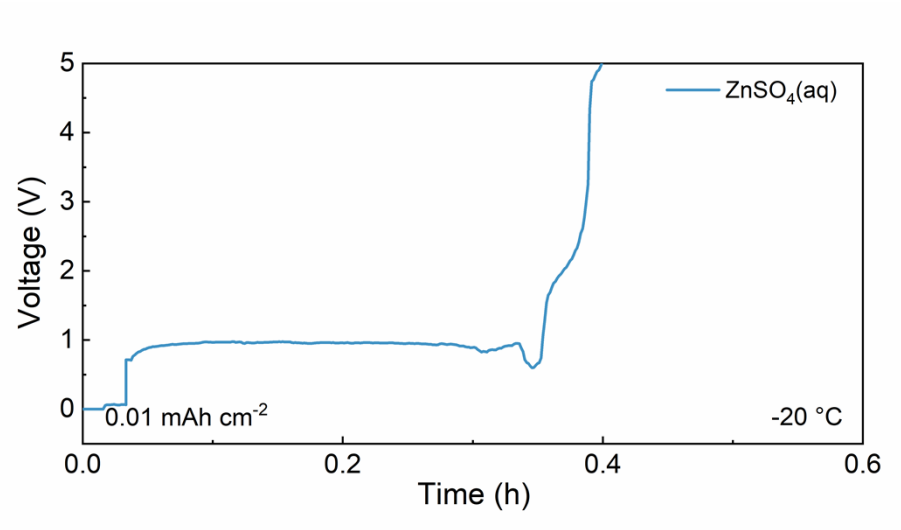

Fig. S29 The voltage profiles of Zn−Zn symmetric cell in $ZnSO_4$ aqueous electrolyte at −20 °C.

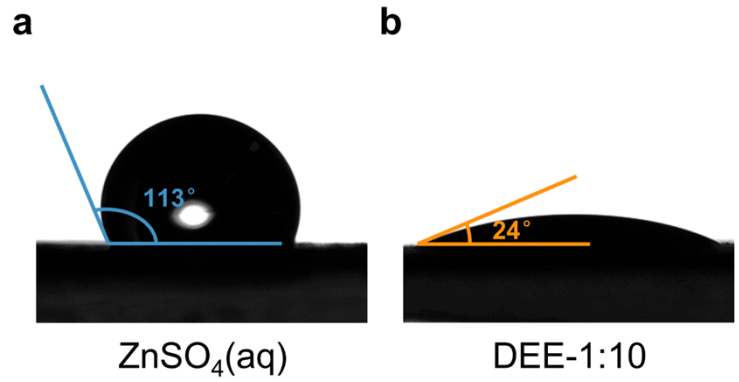

Fig. S30 The solid-liquid contact angle between the V_2O_5 cathode and (a) $ZnSO_4$ aqueous electrolyte and (b) DEE-1:10.

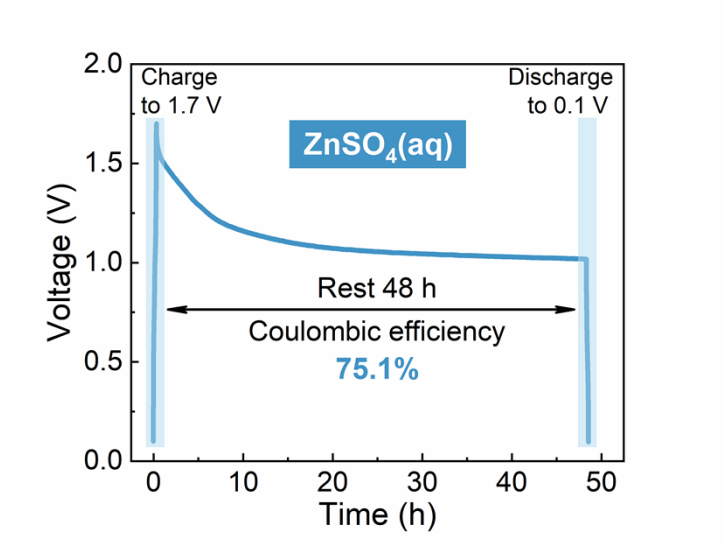

Fig. S31 Self-discharge resistance of Zn−V_2O_5 full cell in $ZnSO_4$ aqueous electrolyte.

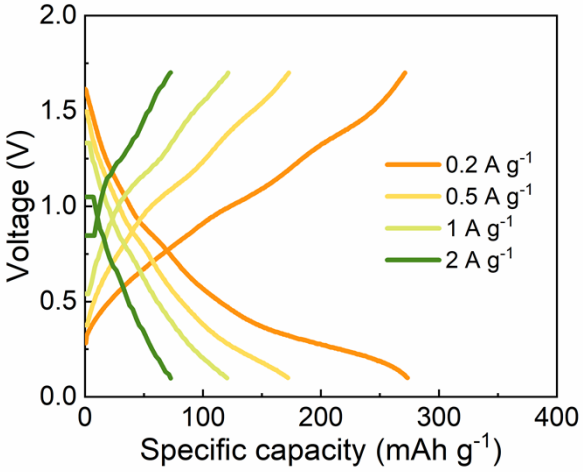

Fig. S32 Corresponding charge-discharge curves of Zn−V_2O_5 full cell in DEE-1:10 at different current densities.

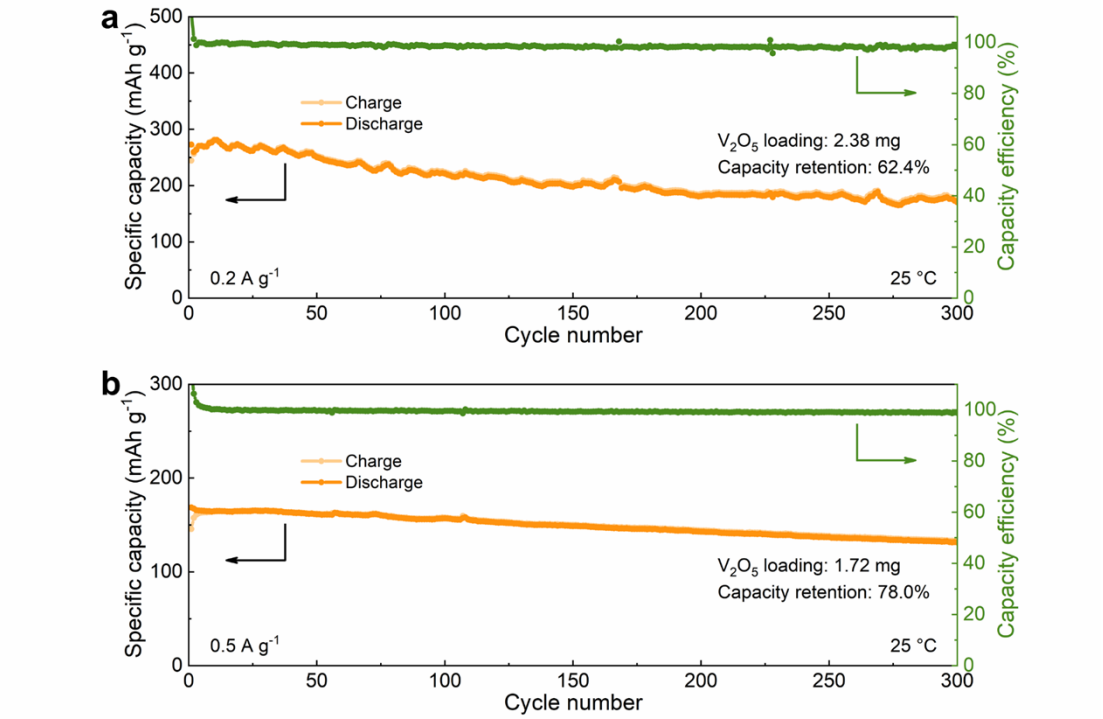

Fig. S33 Cycling performance of Zn−V_2O_5 full cell in DEE-1:10 at (a) 0.2 A g^{-1} and (b) 0.5 A g^{-1}.

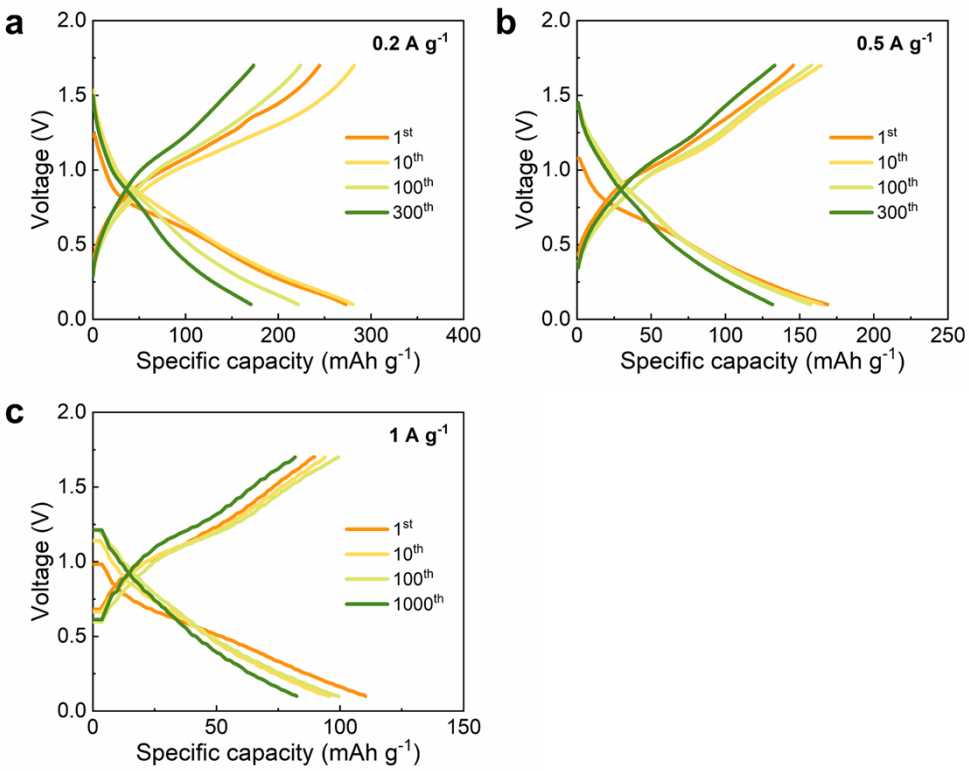

Fig. S34 Corresponding GCD curves of Zn−V_2O_5 full cell in DEE-1:10 at (a) 0.2 A g^{-1}, (b) 0.5 A g^{-1} and (c) 1 A g^{-1} under different cycles.

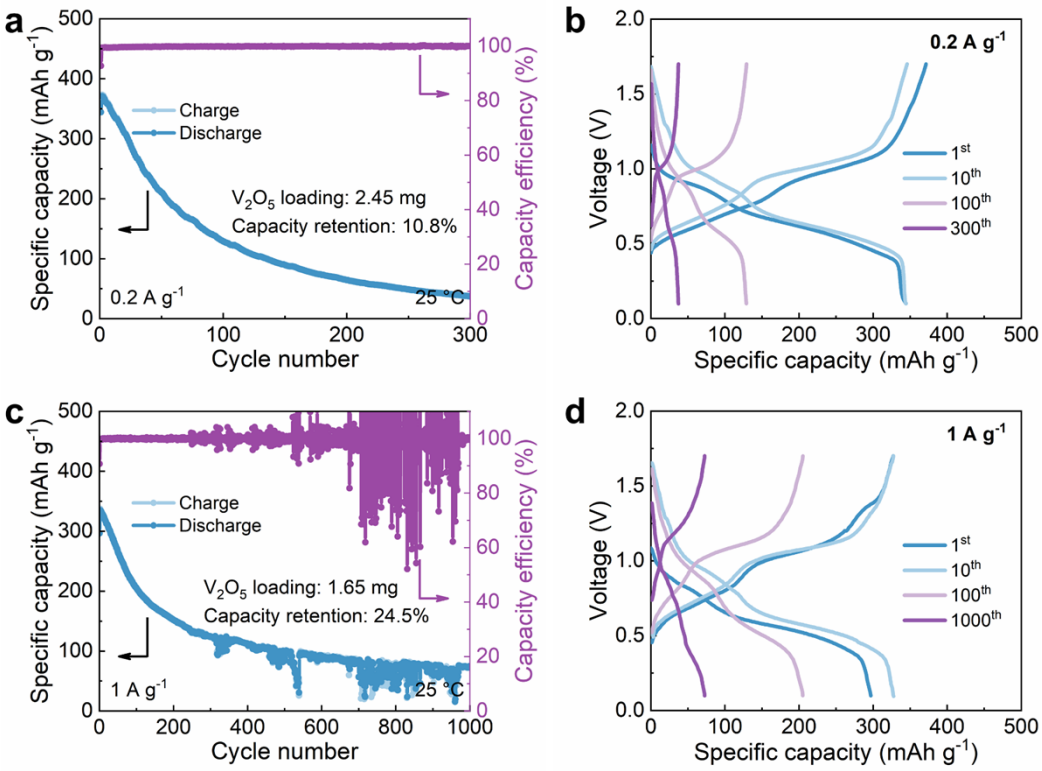

Fig. S35 Cycling performance and corresponding GCD curves of Zn−V_2O_5 full cell in $ZnSO_4$ aqueous electrolyte at (a, b) 0.2 A g^{-1} and (c, d) 1 A g^{-1}.

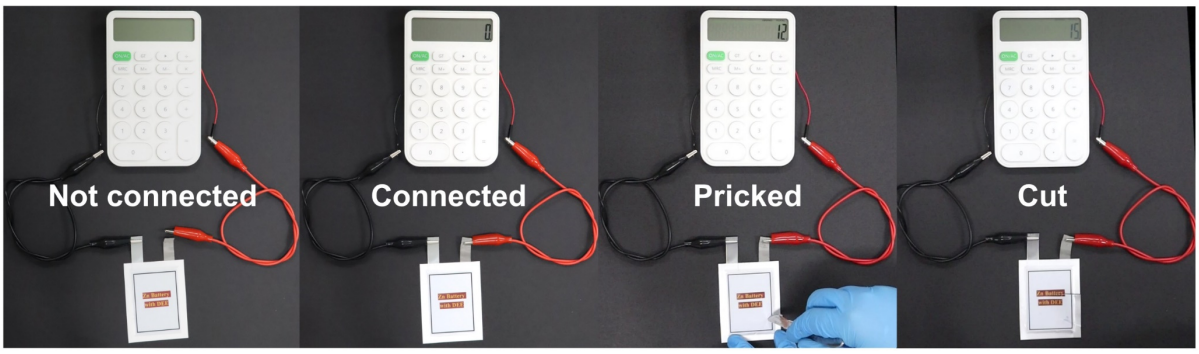

Fig. S36 Pierced and cut tests of Zn−V_2O_5 pouch cell in DEE-1:10.

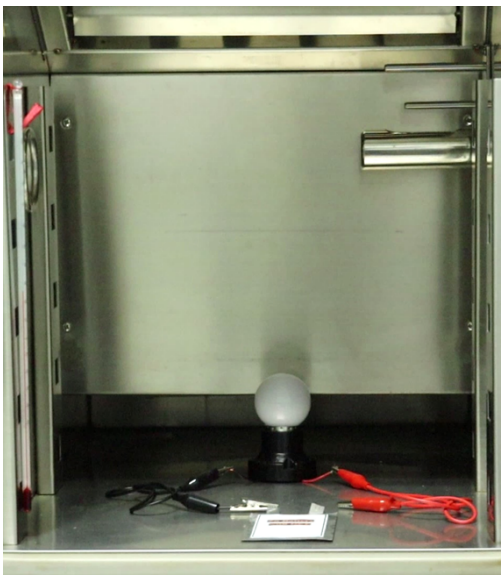

Fig. S37 A night light without power connection.

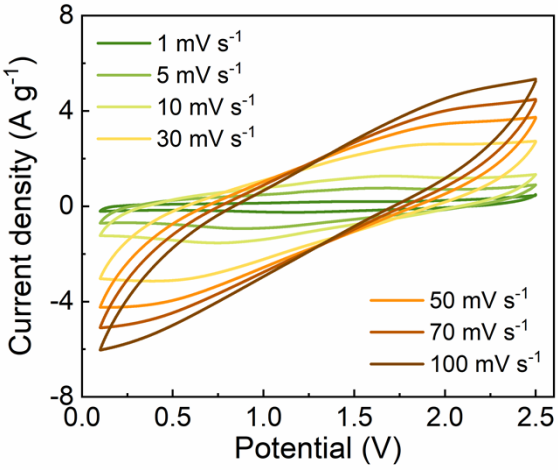

Fig. S38 CV curves of Zn-ion hybrid capacitor with the operating window of 0.1~2.5 V at different scan rates.

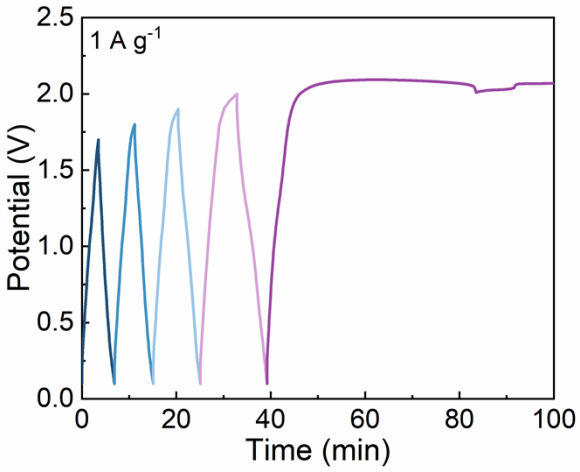

Fig. S39 Corresponding GCD curves of Zn-ion hybrid capacitor using $ZnSO_4$ aqueous electrolyte with different operating windows.

Table S1. Ionic conductivity and viscosity of DEEs with different $Zn(TFSI)_2$:DEPA molar ratios.

Molar ratios	Ionic conductivity (mS cm^{-1})	Viscosity (mPa·s)
1:6	1.17	224
1:8	1.12	126
1:10	1.07	63
1:12	0.95	57

Table S2. The electrochemical performance of DEE based on $Zn(TFSI)_2$ and DEPA compared with other previous works.

Electrolyte	Current density (mA cm^{-2})	Areal capacity (mAh cm^{-2})	Lifespan (h)	Ref.
$Zn(TFSI)_2$:DEPA (molar ratio 1:10)	0.1	0.1	12,000	This work
	1	1	1200	
$Zn(TFSI)_2$:Ace (molar ratio 1:7)	0.1	0.05	1000	10
	1	0.5	100	
$ZnCl_2$:EG (molar ratio 1:4)	0.5	0.5	2000	11
	1	1	3200	
4 m $Zn(BF_4)_2$ + EG	0.5	0.25	4000	12
	1	1	800	
1 M $ZnCl_2$ + ChCl:EG:Urea (molar ratio 1:2:1)	0.1	0.1	3000	13
	0.5	0.5	1400	
Saturated $Zn(OTf)_2$ + PC:H_2O (volume ratio 1:1)	1	1	1600	14
	10	0.5	400	
$Zn(ClO_4)_2 \cdot 6H_2O$:SN (molar ratio 1:8)	0.05	0.5	800	15
	0.2	2	400	
30 m $ZnCl_2$ + 5 m LiCl	1	1	2000	16
	2	4	4000	
4 M $Zn(OTf)_2$ + 2 M $LiClO_4$	2	1	300	17
2 M $ZnSO_4$ + 1 M ESA	0.5	0.5	6000	18
	1	1	2800	
2 M $ZnSO_4$ + 10wt% TFA	5	1	1360	19
	10	1	1100	

Table S3. The physicochemical properties of DEE based on $Zn(TFSI)_2$ and DEPA compared with other previous works.

Electrolyte	Flammability of components	Temperature range (°C)	Operating window (V)	Ref.
$Zn(TFSI)_2$:DEPA (molar ratio 1:10)	Nonflammable	−20~80	0.1~2.5	This work
Saturated $Zn(OTf)_2$ + PC:H_2O (volume ratio 1:1)	Flammable	−20~50	0.8~2.1	[14]
$Zn(ClO_4)_2·6H_2O$:SN (molar ratio 1:8)	Nonflammable	−20~25	0.6~2	[15]
30 m $ZnCl_2$ + 5 m LiCl	Nonflammable	25	0.2~1.6	[16]
4 M $Zn(OTf)_2$ + 2 M $LiClO_4$	Nonflammable	25	0.8~1.4	[17]
2 M $ZnSO_4$ + 1 M ESA	Nonflammable	−10~25	0.2~1.8	[18]
2 M $ZnSO_4$ + 10wt% TFA	Nonflammable	25~70	0.2~1.8	[19]
1 M $Zn(OTf)_2$ + γ-valerolactone	Flammable	−50~80	0.2~1.8	[20]
$Zn(ClO_4)_2·6H_2O$:EG + 50vol% $lnCl_3$ (molar ratio 1:4)	Flammable	−50~50	0.5~1.6	[21]
0.5 M $Zn(OTf)_2$ + DMF	Flammable	−70~80	0.1~1.7	[22]
2 M $Zn(OTf)_2$ + TMU:H_2O (volume ratio 1:3)	Flammable	−30~80	0.2~1.8	[23]
1 m $Zn(OTf)_2$ + G2:H_2O (volume ratio 3:2)	Flammable	−45~60	0.2~1.6	[24]
$(EMIM)_5Zn(OTF)_7$ + EG:H_2O (ratio 3:2)	Flammable	-40~60	0.5~1.6	[25]
$Zn(ClO_4)_2·6H_2O$:SL (molar ratio 1:6)	Nonflammable	−30~20	0.5~1.6	[26]

References

1. C. W. Extrand, *Langmuir*, 2003, **19**, 646-649.
2. J. Zhang, W. Huang, L. Li, C. Chang, K. Yang, L. Gao and X. Pu, *Adv. Mater.*, 2023, **35**, 2300073.
3. S. J. Clark, M. D. Segall, C. J. Pickard, P. J. Hasnip, M. I. J. Probert, K. Refson and M. C. Payne, *Z. Krist-cryst. Mater.*, 2005, **220**, 567-570.
4. J. P. Perdew, K. Burke and M. Ernzerhof, *Phys. Rev. Lett.*, 1996, **77**, 3865-3868.
5. P. J. Hasnip and C. J. Pickard, *Comput. Phys. Commun.*, 2006, **174**, 24-29.
6. J. P. Perdew, J. A. Chevary, S. H. Vosko, K. A. Jackson, M. R. Pederson, D. J. Singh and C. Fiolhais, *Phys. Rev. B*, 1992, **46**, 6671-6687.
7. D. Vanderbilt, *Phys. Rev. B*, 1990, **41**, 7892-7895.
8. J. D. Head and M. C. Zerner, *Chem. Phys. Lett.*, 1985, **122**, 264-270.
9. M. I. J. Probert and M. C. Payne, *Phys. Rev. B*, 2003, **67**, 075204.
10. H. Qiu, X. Du, J. Zhao, Y. Wang, J. Ju, Z. Chen, Z. Hu, D. Yan, X. Zhou and G. Cui, *Nat. Commun.*, 2019, **10**, 5374.
11. L. Geng, J. Meng, X. Wang, C. Han, K. Han, Z. Xiao, M. Huang, P. Xu, L. Zhang, L. Zhou and L. Mai, *Angew. Chem. Int. Ed.*, 2022, **61**, e202206717.
12. D. Han, C. Cui, K. Zhang, Z. Wang, J. Gao, Y. Guo, Z. Zhang, S. Wu, L. Yin, Z. Weng, F. Kang and Q. H. Yang, *Nat. Sustain.*, 2022, **5**, 205-213.
13. W. Li, W. Kong, W. Liu, S. Xu, H. Zhu, S. Liu, W. Yu and Z. Wen, *Energy Storage Mater.*, 2024, **65**, 103103.
14. F. Ming, Y. Zhu, G. Huang, A. H. Emwas, H. Liang, Y. Cui and H. N. Alshareef, *J. Am. Chem. Soc.*, 2022, **144**, 7160-7170.
15. W. H. Yang, X. F. Du, J. W. Zhao, Z. Chen, J. J. Li, J. Xie, Y. J. Zhang, Z. L. Cui, Q. Y. Kong, Z. M. Zhao, C. G. Wang, Q. C. Zhang and G. L. Cui, *Joule*, 2020, **4**, 1557-1574.
16. C. Zhang, W. Shin, L. D. Zhu, C. Chen, J. C. Neuefeind, Y. K. Xu, S. I. Allec, C. Liu, Z. X. Wei, A. Daniyar, J. X. Jiang, C. Fang, P. A. Greaney and X. L. Ji, *Carbon Energy*, 2021, **3**, 339-348.

17. B. W. Olbasa, C. J. Huang, F. W. Fenta, S. K. Jiang, S. A. Chala, H. C. Tao, Y. Nikodimos, C. C. Wang, H. S. Sheu, Y. W. Yang, T. L. Ma, S. H. Wu, W. N. Su, H. Dai and B. J. Hwang, *Adv. Funct. Mater.*, 2022, **32**, 2103959.
18. Y. Wang, R. Zhao, M. Liu, J. Yang, A. Zhang, J. Yue, C. Wu and Y. Bai, *Adv. Energy Mater.*, 2023, **13**, 2302707.
19. M. M. Wu, X. C. Wang, F. Zhang, Q. Xiang, Y. Li and J. X. Guo, *Energy Environ. Sci.*, 2024, **17**, 619-629.
20. C. Xie, S. Liu, W. Zhang, H. Ji, S. Chu, Q. Zhang, Y. Tang and H. Wang, *Angew. Chem. Int. Ed.*, 2023, **62**, e202304259.
21. J. Wan, R. Wang, Z. Liu, S. Zhang, J. Hao, J. Mao, H. Li, D. Chao, L. Zhang and C. Zhang, *Adv. Mater.*, 2024, **36**, 2310623.
22. N. Wang, X. Dong, B. Wang, Z. Guo, Z. Wang, R. Wang, X. Qiu and Y. Wang, *Angew. Chem. Int. Ed.*, 2020, **59**, 14577-14583.
23. X. Yun, Y. Chen, H. Gao, D. Lu, L. Zuo, P. Gao, G. Zhou, C. Zheng and P. Xiao, *Adv. Energy Mater.*, 2024, 2304341.
24. R. Zhang, W. K. Pang, J. Vongsvivut, J. A. Yuwono, G. Li, Y. Lyu, Y. Fan, Y. Zhao, S. Zhang, J. Mao, Q. Cai, S. Liu and Z. Guo, *Energy Environ. Sci.*, 2024.
25. M. Zhong, Y. Wang, Y. Xie, S. Yuan, K. Ding, E. J. Begin, Y. Zhang, J. L. Bao and Y. Wang, *Adv. Funct. Mater.*, 2024, 2316788.
26. X. Lin, G. Zhou, M. J. Robson, J. Yu, S. C. T. Kwok and F. Ciucci, *Adv. Funct. Mater.*, 2022, **32**, 2109322.